Terahertz conductivity of monolayer MoS_2

S. Mitra,* L. Avazpour,† and I. Knezevic‡
Department of Electrical and Computer Engineering,
University of Wisconsin-Madison, Madison, Wisconsin 53706, USA

We calculate the electrical conductivity of suspended and supported monolayer MoS_2 at terahertz (THz) frequencies by means of EMC–FDTD, a multiphysics simulation tool combining an ensemble Monte Carlo (EMC) solver for electron transport and a finite-difference time-domain (FDTD) solver for full-wave electrodynamics. We investigate the role of carrier and impurity densities, as well as substrate choice (SiO_2 or hexagonal boron nitride, hBN), in frequency-dependent electronic transport. Owing to the dominance of surface-optical-phonon scattering, MoS_2 on SiO_2 has the lowest static conductivity, but also the weakest overall frequency dependence of the conductivity. In fact, at high THz frequencies, the conductivity of MoS_2 on SiO_2 exceeds that of either suspended or hBN-supported MoS_2. We extract the parameters for Drude-model fits to the conductivity versus frequency curves obtained from microscopic simulation, which may aid in the experimental efforts toward MoS_2 THz applications.

I. INTRODUCTION

Transition-metal dichalcogenides (TMDs) are widely studied two-dimensional (2D) materials [1–4]. Molybdenum disulfide (MoS_2) is a common example of this group of materials, showing promise for thermal, mechanical, and electronic applications [5–11]. The bandgap of MoS_2 changes from indirect to direct bandgap as the material goes from bulk to single layer [12], which makes monolayer MoS_2 a candidate for a wide range of optoelectronic applications. However, the transfer process from TMD nanolayers onto the substrate impacts its optical and electrical properties [13].

The complex conductivity $\sigma(\omega)$, where ω is the angular frequency, is a response quantity that characterizes electrical transport under low-amplitude ac electrical biasing or excitation by electromagnetic waves. The terahertz (THz) frequency range is interesting for various device applications, but also from the standpoint of fundamental science, because the scattering rates of electrons in many bulk semiconductors and 2D materials fall in this range. There have been experimental measurements of the low-terahertz conductivity of monolayer MoS_2 [14–19]. However, theoretical work on the electronic and optical properties of TMDs in general and MoS_2 in particular in this frequency range is scarce. A key challenge is the need to treat electronic transport and electrodynamics on an equal footing because of the similarity between the excitation frequencies and typical scattering rates, which makes the commonly employed quasistatic approximation for electrodynamics woefully insufficient.

In this paper, we calculate the static and frequency-dependent electrical conductivity for MoS_2 in the terahertz range by employing EMC–FDTD, a multiphysics simulation tool incorporating an ensemble Monte Carlo (EMC) solver for electron transport coupled with a finite-difference time-domain (FDTD) solver for full-wave electrodynamics. This simulation tool has been used to compute the terahertz conductivity of bulk silicon [20–23] and 2D graphene sheets [24–26]. In MoS_2, electron dynamics is governed by the interactions with intrinsic phonons, charged impurities, and substrate phonons. In the static case, the conductivity is nonlinear in electron density owing to dynamical screening, which FDTD captures, and we provide an empirical fit for the mobility versus density dependence. In the case of excitation by an electromagnetic wave, we calculate the complex conductivity as a function of frequency and investigate the role of electron density and substrate choice. We note that the conductivity versus frequency dependencies obtained via EMC–FDTD can be fitted by a Drude model, for which we extract the density-and-substrate-dependent fitting parameters. The empirical fits arising from our detailed

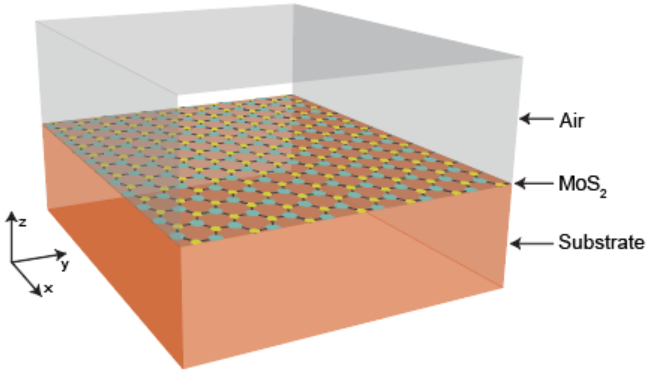

FIG. 1. Schematic of the three-dimensional (3D) simulation geometry. A TEM plane wave polarized in the y-direction excites electrons in the MoS_2 layer. The four vertical boundaries of the simulation domain (parallel to the x–z and y–z planes) are terminated with periodic boundary conditions, while the horizontal boundaries at the top and bottom (parallel to the x–y plane) are terminated with the convolutional perfectly matched layer (CPML) absorbing boundary condition.

* smitra8@wisc.edu
† laleh.avazpour@wisc.edu
‡ iknezevic@wisc.edu

multiphysics microscopic simulation may benefit further experimental efforts in the application of 2D materials for terahertz-based devices and integrated circuits, sensors, and detectors.

The the paper is organized as follows. In Sec. II, we overview the coupled EMC–FDTD technique and its implementation. In Sec. III, we focus on the band structure and scattering mechanisms relevant in carrier transport. In IV, we present our findings on the static (dc) and terahertz conductivity of MoS_2 that is suspended, as well as on SiO_2 and hBN substrates. We conclude in Sec. V.

II. NUMERICAL TECHNIQUE

This section provides a brief introduction to our multiphysics EMC–FDTD solver used for computing the frequency-dependent low-field carrier transport; more details can be found in the previously published technique papers [22, 24].

Ensemble Monte Carlo (EMC) is a stochastic technique used to solve the Boltzmann equation for electron transport, which is appropriate in the semiclassical transport regime and under the assumptions that no interband transitions occur as a result of excitation (fulfilled in the THz frequency range). In a typical EMC simulation, a large number of charge carriers are tracked over time as they drift and scatter under the relevant scattering mechanisms. During drift, each carrier accelerates under the influence of the electric and magnetic fields according to the Lorentz force:

$$\mathbf{F} = e\left(\mathbf{E} + \mathbf{v} \times \mathbf{B}\right), \tag{1}$$

where $\mathbf{E}$ and $\mathbf{B}$ are the electric and magnetic fields, e is the electron charge, and $\mathbf{v}$ is the carrier velocity. For a parabolic band with an isotropic effective mass m^*, $\mathbf{v} = \frac{\hbar^2\mathbf{k}}{m^*}$, where $\mathbf{k}$ is the wave vector. The free-flight duration t_d between successive scattering events is calculated with the aid of a random number r and the maximal cumulative scattering rate Γ for the relevant electron energy range as $t_d = -\ln(r)/\Gamma$ [27].

The real-space position, momentum, and energy of the carrier are updated according to Newton's second law with the Lorentz force and the energy–momentum relationship captured through the full electronic band structure of the material:

$$\mathbf{r}_{\text{new}} = \mathbf{r}_{\text{old}} + \int_0^{t_d} \mathbf{v}(t)dt, \tag{2}$$

$$\mathbf{k}_{\text{new}} = \mathbf{k}_{\text{old}} + \frac{1}{\hbar}\int_0^{t_d} \mathbf{F}\left(\mathbf{r}(t)\right)dt, \tag{3}$$

$$E = \frac{\hbar^2}{2m^*}|\mathbf{k}_{\text{new}}|^2. \tag{4}$$

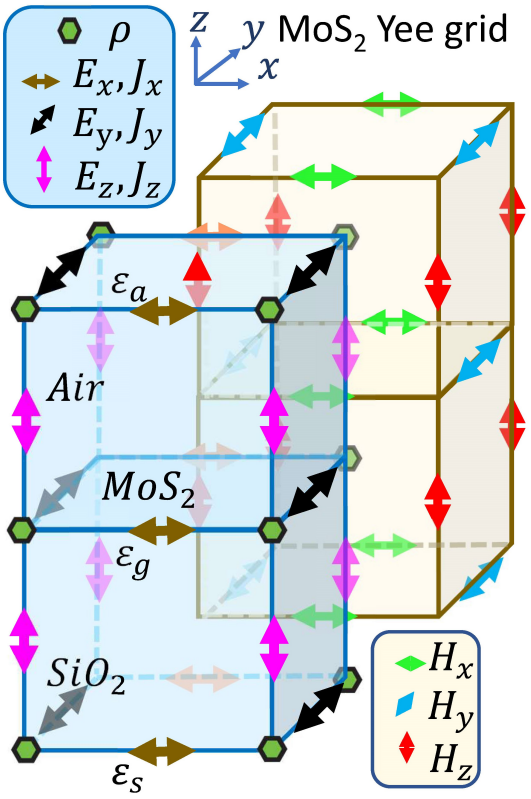

FIG. 2. The Yee cell and field assignment near the air/MoS_2/SiO_2 interface. MoS_2 lies in the central plane, sandwiched between half-spaces filled with air on top and substrate on the bottom. $\mathbf{E}$ and $\mathbf{H}$ field are staggered in space. ($\mathbf{E}$, $\mathbf{J}$) and ($\mathbf{H}$, $\mathbf{M}$) are collocated. Note the location of the charge density ρ, which is not present in standard FDTD implementations, but is critical for multiphysics simulations involving electron transport.

The finite-difference time-domain (FDTD) method [28] is a popular time-dependent technique for solving Maxwell's curl equations

$$\mu\frac{\partial \mathbf{H}}{\partial t} = -\nabla \times \mathbf{E} - \mathbf{M}, \tag{5}$$

$$\epsilon\frac{\partial \mathbf{E}}{\partial t} = \nabla \times \mathbf{H} - \mathbf{J}, \tag{6}$$

using a finite-difference scheme for the partial derivatives in both space and time. It relies on the Yee grid (Fig. 2) where the field components of $\mathbf{E}$ and $\mathbf{H} = \mu^{-1}\mathbf{B}$ are spatially staggered by half a grid cell. Using the leapfrog integration scheme, we update the fields, which are also staggered by half a time step.

However, in contrast to standard FDTD that is employed in media without free charges (so the curl equations suffice), our FDTD must keep track of the nonzero microscopic charge distribution. Namely, the coupled

EMC–FDTD simulation starts off with a carrier ensemble initialized based on the thermal distribution. The impurity ions are randomly distributed in the MoS_2 layer and the substrate [26]. Based on the position of the electrons and charged impurities, Poisson's equation

$$\nabla^2\phi = -\frac{\rho}{\epsilon} \tag{7}$$

must is solved to calculate the initial electric-field distribution. Solving Poisson's equation at initialization ensures that Gauss's law is satisfied at that time, and enforcing the charge–current continuity equation

$$\nabla \cdot \mathbf{J} = -\frac{\partial \rho}{\partial t}, \tag{8}$$

at subsequent timesteps ensures that Gauss's law is always satisfied [22]. As the EMC module drifts and scatters electrons, we use the Villasenor-Buneman charge-conserving scheme [22, 24, 29] to appropriately assign each electron's contribution to the current density $\mathbf{J}$ at relevant grid cells. $\mathbf{J}$ is then used in the FDTD curl equations to updated electric and magnetic fields and calculate the conductivity. More details can be found in [22, 24].

Figure 2 shows the Yee grid and the FDTD field assignment above and below the MoS_2 layer. E_x and E_y lie in the $(k \pm 1)$-th plane and E_z in $(k \pm \frac{1}{2})$-th plane. The position of the components of $\mathbf{H}$ is reversed. The top half is assumed to be air and the bottom half is updated according to the substrate material properties [30].

In order to simulate a large semiconductor, periodic boundary conditions are assumed for the vertical boundaries of the simulation domain (parallel to the x–z and y–z planes). Fields at top and bottom (horizontal boundaries, parallel to the x–y plane) are absorbed via the convolutional perfectly matched layer (CPML) boundary condition [24].

The incident plane-wave electric field is introduced via the total-field scattered-field (TFSF) framework [22]. The electric and magnetic currents ($\mathbf{J}$ and $\mathbf{M}$) needed to launch the plane wave are introduced at the TFSF boundaries and calculated via the surface equivalence principle.

The complex conductivity $\sigma(\omega)$ is calculated from

$$\sigma(\omega) = \frac{\tilde{\mathbf{E}}(\omega) \cdot \tilde{\mathbf{J}}^*(\omega)}{\left|\tilde{\mathbf{E}}(\omega)\right|^2}, \tag{9}$$

where $\tilde{\mathbf{E}}(\omega)$ and $\tilde{\mathbf{J}}(\omega)$ are the spatially averaged electric-field and current-density phasors in the sinusoidal steady state, respectively.

A more in-depth discussion regarding the requirements for the coupling of EMC and FDTD can be found in Refs. [22, 24].

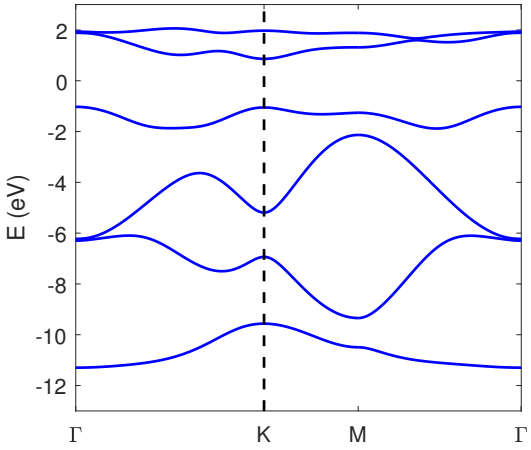

FIG. 3. The band structure of monolayer MoS_2 calculated via an eleven-orbital tight-binding method [31, 32]. Six relevant bands are shown (the Fermi level is at zero). Near the K point, the band structure is parabolic, with an isotropic effective mass $m^* = 0.51m_0$.

III. BAND STRUCTURE AND SCATTERING RATES

The conduction band of monolayer MoS_2, shown in Fig. 3, is calculated via an eleven-orbital tight-binding method [31, 32]. Near the K point, the conduction band can be approximated as parabolic, with an isotropic effective mass $m^* = 0.51m_0$, where m_0 is the free-electron rest mass.

MoS_2 is a polar material. The dominant scattering mechanisms at room temperature are acoustic-phonon scattering and optical-phonon scattering, the latter including both nonpolar and polar (Frölich) types. If the monolayer MoS_2 is on top of a substrate, scattering from surface-optical (SO) phonons should also be included. Ionized impurities might also appear in the material or substrate during processing and should be included as an additional source of scattering.

In our simulation, we assumed all electrons reside in the K valleys. Although additional Q valleys may be energetically relevant, the K–Q valley energy gap has been debated [33]. At low fields (0.1 kV/cm in our simulation), the contribution can be neglected [34]. In addition, SO phonon scattering puts an additional limit on the occupancy in Q valleys [34].

Under the elastic and equipartition approximations, the acoustic-phonon scattering rate is given by [35],

$$\Gamma_{\mathrm{ac}}(k) = \frac{D_{\mathrm{ac}}^2 k_B T m^*}{\hbar^3 \rho_s v_s^2}. \tag{10}$$

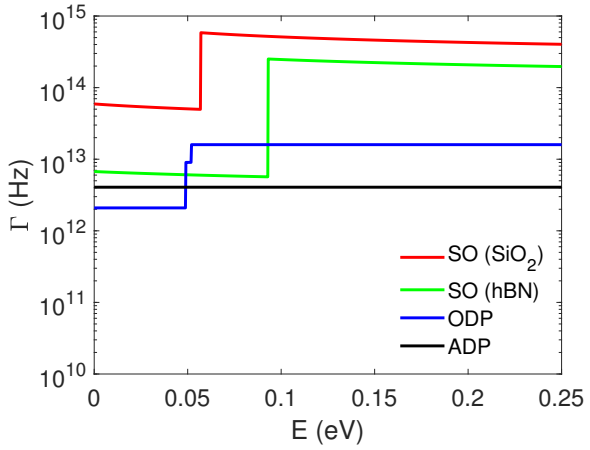

FIG. 4. Electron–phonon scattering rates for monolayer MoS_2 on hBN and SiO_2 substrates. The acoustic-phonon scattering rate is averaged over LA and TA phonons [35]. Optical phonons include both polar and nonpolar contributions. The kink indicates the onset of optical-phonon emission.

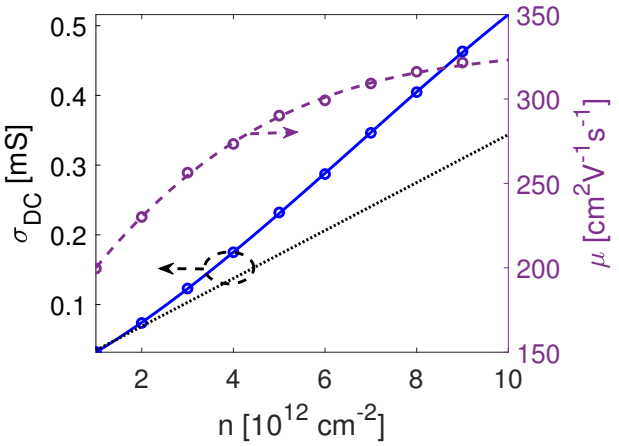

FIG. 5. Static (dc) conductivity of suspended monolayer MoS_2 as a function of electron density. The impurity density is $10^{12}\,\mathrm{cm}^{-2}$. The dotted black line depicts the reference conductivity with unscreened impurities. The solid blue curve presents the conductivity with screened impurities, as obtained from our microscopic multiphysics EMC–FDTD simulation. The dashed purple curve presents the corresponding electron mobility μ whose values can be read off the right vertical axis. At low carrier densities, transport is limited by the weakly screened ionized impurities. At higher densities, the screening effect becomes significant, and the mobility value obtained from our solver approaches the impurity-free value of $\sim 320\ \mathrm{cm}^{-2}\mathrm{V}^{-1}\mathrm{s}^{-1}$.

The optical-phonon scattering rate is given by

$$\Gamma_{\mathrm{op}}(k) = \frac{D_{\mathrm{op}}^2 g_d m^*}{2\hbar^2 \rho_s \omega_{\mathrm{op}}} \left[N_q + (N_q+1)\Theta(E-\hbar\omega_{\mathrm{op}})\right], \quad (11)$$

where N_q is the Bose-Einstein distribution function and $\Theta(x)$ is the Heaviside step function that indicates the threshold for optical-phonon emission. While scattering of electrons with optical phonons generally includes both polar and nonpolar components, and polar-optical-phonon scattering in TMDs has been subject to extensive study in first principles calculations. In all, the deformation-potential approximation appears to provide a satisfactory description of electron–optical-phonon coupling for the purposes of electrons transport at low fields, which is why we adopt it in Eq. (11).

Using the interaction Hamiltonian theory [36], the rate of electron scattering with remote SO phonons is [30]

$$\Gamma_{\mathrm{so}}(k) = \frac{32\pi^3 e^2 F_v^2 m^* S}{\hbar^3 a^2} \left(N_q + \frac{1}{2} \pm \frac{1}{2}\right) \times \int_{-\pi}^{\pi} \frac{1}{q} \frac{\sinh\left(\frac{aq}{2}\right)}{\left(4\pi^2 q + a^2 q^3\right)^2} d\theta. \quad (12)$$

The electron–SO phonon coupling parameter is

$$F_v^2 = \frac{\hbar\omega_{\mathrm{so}}}{2S\epsilon_0} \left(\frac{1}{\epsilon_{\mathrm{ox}}^{\infty} + \epsilon_{\mathrm{ox}'}^{\infty}} - \frac{1}{\epsilon_{\mathrm{ox}}^{0} + \epsilon_{\mathrm{ox}'}^{\infty}}\right), \quad (13)$$

where ω_{so} is the SO-phonon frequency, $\epsilon_{\mathrm{ox}}^{\infty}$ ($\epsilon_{\mathrm{ox}}^{0}$) is the high-frequency (low-frequency) dielectric constant of the substrate, and $\epsilon_{\mathrm{ox}'}^{\infty}$ is the high-frequency dielectric constant of the top dielectric (here, it is air). It has been argued that hybrid interface-plasmon/SO-phonon excitations might exist [37], but we did not consider such hybrid modes in our calculations. We assumed dispersionless SO phonons. We chose SiO_2 and hBN substrates as commonly used polar substates. The material parameters were taken from [30] and [38].

While Fermi's golden rule is used to calculate the acoustic and optical-phonon scattering rates, modeling the effect of ionized impurities with rates tends to overestimate their effect on transport [22, 39]. Our multiphysics tool incorporates a real-space distribution of ionized impurities, and the FDTD module handles the long-range (grid-cell-size and above) component of the electron–ion interaction, including the effects of dynamical screening. The short-range (sub-grid-cell-size) interaction can be included via the molecular dynamics (MD) addition to the EMC–FDTD solver [26], but the computation burden is high and not routinely warranted. In the absence of the MD add-on, choosing a smaller grid-cell size would result in more accurate fields, but such choice also significantly increases runtime. Our chosen grid-cell size is 5 nm, balancing accuracy with computational cost.

IV. RESULTS

The static (dc) conductivity of suspended monolayer MoS_2 as a function of the sheet carrier density is shown in Fig. 5. This carrier density should be considered the spatial average corresponding to a given Fermi level; the actual microscopic density is generally nonuniform. The

ionized impurity density is fixed at $10^{12}\,\mathrm{cm}^{-2}$, which is also the average value, while the impurities are randomly distributed according to a uniform distribution. For unscreened impurities, the σ_{dc} $(= en\mu_{\mathrm{dc}})$ is expected to be linear, as mobility μ is virtually independent of the carrier density in this region [35]; the dotted black line in Fig. 5 represents this unscreened conductivity as a reference. In our microscopic multiphysics simulation, we obtain a nonlinear relationship between conductivity and density, which can be attributed to electron-density-dependent screening of ionized impurities. This dc mobility of suspended monolayer MoS_2 can be approximated by the empirical relation, $\mu_{\mathrm{dc}} = -1.683n^2 + 31.59n + 172.8$, where μ is in $\mathrm{cm}^{-2}\mathrm{V}^{-1}\mathrm{s}^{-1}$, n in 10^{12} cm^{-2}, and 10^{12} $\mathrm{cm}^{-2} \leq n \leq 10^{13}$ cm^{-2}. Our result shows the impurities are mostly screened for a carrier-to-impurity ratio of 10, as evidenced by the fact that the mobility value obtained from our solver approaches the impurity-free value of ~ 320 $\mathrm{cm}^{-2}\mathrm{V}^{-1}\mathrm{s}^{-1}$. However, it should be noted that beyond the carrier density of 10^{13} cm^{-2}, the electron–electron interaction may be significant, which requires additional modeling details not currently included in the simulation (such as the short-range (sub-grid-cell) direct and exchange interactions, which the solver can treat in principle using the computationally costly MD addition[26]).

The real part of $\sigma(\omega)$ for the pure monolayer MoS_2 is shown in Figure 6 at different carrier densities. The result shows Drude-like conductivity in the terahertz region.

The Drude model for the conductivity can be written as

$$\sigma(\omega) = \frac{\sigma_{\mathrm{dc}}}{1 - i\omega\tau}, \tag{14}$$

where τ is an effective relaxation time. The Drude model works well when the microscopic energy-resolved momentum-relaxation time is independent of the carrier energy, as is the case, for example, with typical "dirty" bulk metals. In contrast, MoS_2 is a high-quality material, but with an approximately constant density of states owing to its 2D nature. As a result, the phonon scattering rates are constant as functions of energy, aside from the weak $1/q$ dependence for SO-phonon scattering, which bodes well for a Drude-type response. The effective τ from the Drude fit is limited by ionized impurity scattering at low densities. As the carrier density increases, τ approaches the impurity-free relaxation time of ~ 90 fs. τ can be approximated by the empirical formula $\tau = -0.34n^2 + 7.4n + 51.14$, where τ is in fs, n in 10^{12} cm^{-2}, and 10^{12} $\mathrm{cm}^{-2} \leq n \leq 10^{13}$ cm^{-2}.

In Fig. 7, we show the frequency-dependent conductivity of supported and suspended monolayer MoS_2 for the carrier density of 5×10^{12} cm^{-2}. The frequency of terahertz excitation is varied from 500 GHz to 10 THz. Both the suspended and supported MoS_2 (substrates are SiO_2 or hBN) show Drude-like conductivity in the terahertz frequency range, arguably because of the weak dependence of the scattering rates on carrier energy, which

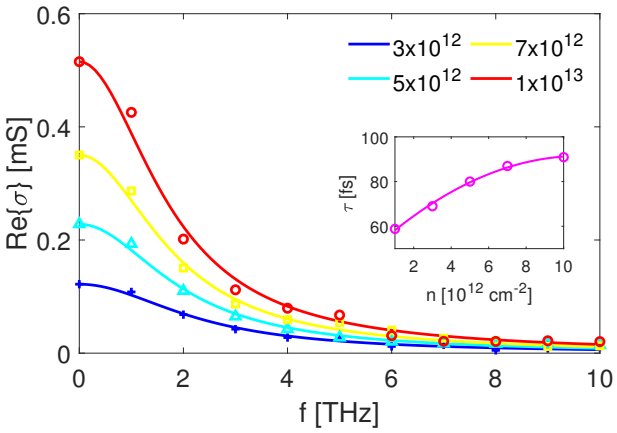

FIG. 6. Real part of $\sigma(\omega)$ as a function of terahertz frequency for different electron densities in suspended monolayer MoS_2. The dots, squares, triangles, and stars correspond to the conductivity calculated by EMC–FDTD. The solid lines correspond to Drude fits. The inset shows the effective carrier lifetime τ of the Drude fits as a function of the electron density. τ versus electron density saturates at ~ 90 fs. The impurity density throughout is 10^{12} cm^{-2}.

stems from the material's 2D nature. For the suspended case, the only scattering mechanisms are those between electrons and the material's intrinsic acoustic and optical phonons, and these rates are comparable to one another in magnitude, with values of around 10 THz (see Fig. 6). For supported cases, the SO phonon scattering is dominant by over an order of magnitude over the other two mechanisms, and the rates lie closer to the PHz frequency range. While a suspended layer's dc conductivity is higher than that of a supported one, the effective scattering rate for the suspended case is comparable to the excitation frequency, which is why we see a sharp fall of the value of conductivity at higher frequencies. In the supported cases, the dc or low-frequency conductivity is lower because SO-phonon scattering is the dominant process. While hBN is a weak polar material whose effective scattering rate lies in the upper terahertz region, SiO_2 is a highly polar material whose rate is well above the THz range. As a result, the dc conductivity of the SiO_2 supported layer is the smallest of the three, but it also remains flat as a function of frequency. The hBN result is in between the suspended and SiO_2 ones. Compared to the relaxation time for suspended MoS_2, the relaxation times for hBN and SiO_2 substrates are about 1.6 times and 5 times lower, respectively. Because of the contrast between the relaxation times, above 4.5 THz, the more polar SiO_2 substrate, whose $\omega\tau < 1$, actually retains conductivity better than the less polar hBN substrate or even the ideal suspended case. The result is perhaps not obvious, but is interesting for THz applications. The calculated mobility of electrons in MoS_2 on SiO_2 is in the range 40–100 $\mathrm{cm}^2\mathrm{V}^{-1}\mathrm{s}^{-1}$, which agrees with the previously reported values [40, 41]. The Drude

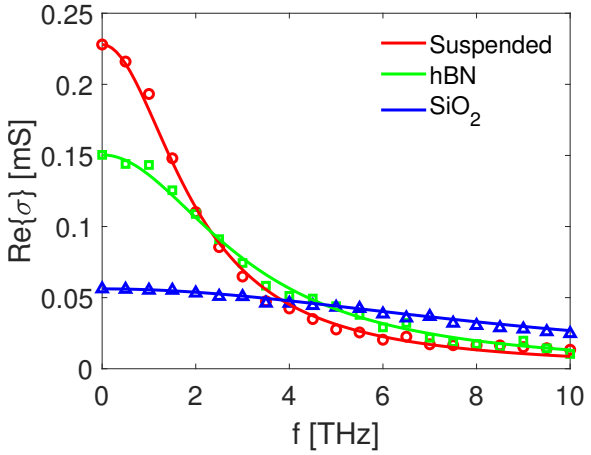

FIG. 7. Real part of $\sigma(\omega)$ as a function of terahertz frequency. The dots, squares, and triangles correspond to the conductivity calculated by EMC–FDTD for MoS_2 suspended, supported on hBN, and supported on SiO_2, respectively. The solid lines are Drude fits.

model parameters for the three cases are given in Table I.

While our simulations show a Drude-type conductivity of MoS_2 throughout the THz frequency range, experimental data for the conductivity at frequencies below 3 THz [14–19] follows the Drude-Smith formula [42],

$$\sigma(\omega) = \frac{\sigma_{\rm dc}}{1 - i\omega\tau}\left[1 + \frac{c}{1 - i\omega\tau}\right], \qquad (15)$$

where the factor c is the Smith contribution, known as the backscattering or localization parameter and having a value between 0 and -1 ($c = -1$ corresponds to coherent backscattering that can lead to localization, while $c = 0$ corresponds to random phase-destroying scattering events characteristic of the Drude model). The Drude–Smith formula is used to describe the conductivity of layered-alloy and disordered media [43]. For TMDs under low-THz frequencies, it has been argued that the effects from many-body effects such as excitons and trions may contribute to this localization correction [14, 44, 45]. The polycrystallinity of TMD samples This has also been associated with the Smith contribution [18]. In all, a microscopic description of the backscattering contribution to conductivity below 3 THz is still being developed. Our simulation tool does not capture many-body or other coherent effects (since EMC is purely semiclassical) and we assume single-crystalline samples. Nonetheless, our work should accurately capture the experimentally observed conductivity above 3 THz. Below 3 THz, our results could be used as a reference Drude value when extracting the extent of the many-body effects by subtracting the Drude contribution from the experimental results.

TABLE I. Drude-model fitting parameters for the terahertz conductivity of monolayer MoS_2 (suspended and supported on different substrates) for the impurity density 10^{12} cm^{-2}.

Substrate	n (cm^{-2})	$\sigma_{\rm dc}$ (mS)	τ (fs)
–	3×10^{12}	0.1219	68.97
–	5×10^{12}	0.2280	80.00
–	7×10^{12}	0.3503	86.00
–	10×10^{12}	0.5152	90.91
hBN	5×10^{12}	0.1504	51.28
SiO_2	5×10^{12}	0.0562	16.67

V. CONCLUSION

In summary, we calculated the dc and ac conductivity of monolayer MoS_2 using EMC–FDTD, a self-consistent multiphysics numerical tool coupling carrier transport with full-wave electrodynamics. We incorporated the effect of phonons, charged impurities, and substrates (hBN and SiO_2) in the calculation of the frequency-dependent electrical conductivity in the THz range. Our results demonstrate a Drude-like behavior of the conductivity owing to the weak dependence of the scattering rates on energy that arises from the material's 2D nature. The inclusion of the substrate reduces the dc conductivity because the SO-phonon scattering rates are high. However, these high SO-phonons scattering rates also result in MoS_2 on the polar SiO_2 substrate having virtually frequency-independent conductivity, which ends up exceeding the conductivity of either suspended MoS_2 or MoS_2 on the less polar hBN substrate at high THz frequencies.

In conclusion, our microscopic simulation can help us understand the dependencies of electronic transport on density, substrate, and frequency. It also enables us to extract accurate parameters for analytical models that can help predict or analyze the results of new experiments. The numerical technique can be readily applied to calculate the terahertz conductivity of different TMDs and other novel 2D materials and give guidance for substrate engineering.

[1] B. Radisavljevic, A. Radenovic, J. Brivio, V. Giacometti, and A. Kis, Single-layer MoS2 transistors, Nature Nanotechnology **6**, 147 (2011).
[2] S. Manzeli, D. Ovchinnikov, D. Pasquier, O. V. Yazyev, and A. Kis, 2d transition metal dichalcogenides, Nature Reviews Materials **2** (2017).
[3] M. Chhowalla, H. S. Shin, G. Eda, L.-J. Li, K. P. Loh, and H. Zhang, The chemistry of two-dimensional layered transition metal dichalcogenide nanosheets, Nature Chemistry **5**, 263 (2013).

[4] Z. Wei, B. Li, C. Xia, Y. Cui, J. He, J.-B. Xia, and J. Li, Various structures of 2d transition-metal dichalcogenides and their applications, Small Methods **2**, 1800094 (2018).

[5] A. I. Khan, P. Khakbaz, K. A. Brenner, K. K. H. Smithe, M. J. Mleczko, D. Esseni, and E. Pop, Large temperature coefficient of resistance in atomically thin two-dimensional semiconductors, Applied Physics Letters **116**, 203105 (2020).

[6] H. Yuan, X. Liu, L. Ma, Z. Yang, H. Wang, J. Wang, and S. Yang, Application of two-dimensional MoS2 nanosheets in the property improvement of polyimide matrix: Mechanical and thermal aspects, Composites Part A: Applied Science and Manufacturing **95**, 220 (2017).

[7] G. Fiori, F. Bonaccorso, G. Iannaccone, T. Palacios, D. Neumaier, A. Seabaugh, S. K. Banerjee, and L. Colombo, Electronics based on two-dimensional materials, Nature Nanotechnology **9**, 768 (2014).

[8] A. G. Kelly, T. Hallam, C. Backes, A. Harvey, A. S. Esmaeily, I. Godwin, J. Coelho, V. Nicolosi, J. Lauth, A. Kulkarni, S. Kinge, L. D. A. Siebbeles, G. S. Duesberg, and J. N. Coleman, All-printed thin-film transistors from networks of liquid-exfoliated nanosheets, Science **356**, 69 (2017).

[9] D. Lembke, S. Bertolazzi, and A. Kis, Single-layer mos_2 electronics, Accounts of Chemical Research **48**, 100 (2015).

[10] D. Rus and M. T. Tolley, Design, fabrication and control of soft robots, Nature **521**, 467 (2015).

[11] A. Chortos, J. Liu, and Z. Bao, Pursuing prosthetic electronic skin, Nature Materials **15**, 937 (2016).

[12] K. F. Mak, C. Lee, J. Hone, J. Shan, and T. F. Heinz, Atomically thin mos_2: A new direct-gap semiconductor, Phys. Rev. Lett. **105**, 136805 (2010).

[13] S. E. Barker, S. Wang, R. H. Godiksen, G. W. Castellanos, M. Berghuis, T. V. Raziman, A. G. Curto, and J. G. Rivas, Preserving the emission lifetime and efficiency of a monolayer semiconductor upon transfer, Advanced Optical Materials **7**, 1900351 (2019).

[14] C. J. Docherty, P. Parkinson, H. J. Joyce, M.-H. Chiu, C.-H. Chen, M.-Y. Lee, L.-J. Li, L. M. Herz, and M. B. Johnston, Ultrafast transient terahertz conductivity of monolayer mos_2 and ws_2 grown by chemical vapor deposition, ACS Nano **8**, 11147 (2014).

[15] S. Chen, F. Fan, Y. Miao, X. He, K. Zhang, and S. Chang, Ultrasensitive terahertz modulation by silicon-grown mos_2 nanosheets, Nanoscale **8**, 4713 (2016).

[16] X. Yan, L. Zhu, Y. Zhou, Y. E, L. Wang, and X. Xu, Dielectric property, Applied Optics **54**, 6732 (2015).

[17] S. Kar, J. Lake, S. Adeyemo, T. Santra, and H. Joyce, The physics of terahertz negative photoconductivity in low-dimensional materials, Materials Today Physics **23**, 100631 (2022).

[18] M. D. Capobianco, S. M. Younan, U. Tayvah, B. Pattengale, J. Neu, J. Gu, and G. W. Brudvig, Terahertz conductivity of semiconducting 2h and metallic 1t phases of molybdenum disulfide, The Journal of Physical Chemistry Letters **13**, 8319 (2022).

[19] X. Xing, L. Zhao, Z. Zhang, X. Lin, Y. Yu, Z. Jin, W. Liu, W. Zhang, and G. Ma, The modulation of terahertz photoconductivity in CVD grown n-doped monolayer mos_2 with gas adsorption, Journal of Physics: Condensed Matter **31**, 245001 (2019).

[20] K. J. Willis, J. S. Ayubi-Moak, S. C. Hagness, and I. Knezevic, Global modeling of carrier-field dynamics in semiconductors using EMC–FDTD, Journal of Computational Electronics **8**, 153 (2009).

[21] K. J. Willis, S. C. Hagness, and I. Knezevic, Terahertz conductivity of doped silicon calculated using the ensemble monte carlo/finite-difference time-domain simulation technique, Applied Physics Letters **96**, 062106 (2010), https://doi.org/10.1063/1.3308491.

[22] K. J. Willis, S. C. Hagness, and I. Knezevic, Multiphysics simulation of high-frequency carrier dynamics in conductive materials, Journal of Applied Physics **110**, 063714 (2011).

[23] K. J. Willis, S. C. Hagness, and I. Knezevic, A generalized drude model for doped silicon at terahertz frequencies derived from microscopic transport simulation, Applied Physics Letters **102**, 122113 (2013), https://doi.org/10.1063/1.4798658.

[24] N. Sule, K. J. Willis, S. C. Hagness, and I. Knezevic, EMC/FDTD/MD simulation of carrier transport and electrodynamics in two-dimensional electron systems, Journal of Computational Electronics **12**, 563 (2013).

[25] N. Sule, K. J. Willis, S. C. Hagness, and I. Knezevic, Terahertz-frequency electronic transport in graphene, Physical Review B **90**, 10.1103/physrevb.90.045431 (2014).

[26] N. Sule, S. C. Hagness, and I. Knezevic, Clustered impurities and carrier transport in supported graphene, Phys. Rev. B **89**, 165402 (2014).

[27] K. Tomizawa, *Numerical simulation of submicron semiconductor devices*, Electronic Materials & Devices Library (Artech House, Norwood, MA, 1993).

[28] A. Taflove and S. Hagness, *Computational Electrodynamics: The Finite-Difference Time-Domain Method*, 3rd ed. (Artech House, Norwood, 2005).

[29] J. Villasenor and O. Buneman, Rigorous charge conservation for local electromagnetic field solvers, Computer Physics Communications **69**, 306 (1992).

[30] N. Ma and D. Jena, Charge scattering and mobility in atomically thin semiconductors, Physical Review X **4**, 10.1103/physrevx.4.011043 (2014).

[31] J. Silva-Guillén, P. San-Jose, and R. Roldán, Electronic band structure of transition metal dichalcogenides from ab initio and slater–koster tight-binding model, Applied Sciences **6**, 284 (2016).

[32] E. Cappelluti, R. Roldán, J. A. Silva-Guillén, P. Ordejón, and F. Guinea, Tight-binding model and direct-gap/indirect-gap transition in single-layer and multilayer MoS_2, Physical Review B **88**, 10.1103/physrevb.88.075409 (2013).

[33] S. Poncé, W. Li, S. Reichardt, and F. Giustino, First-principles calculations of charge carrier mobility and conductivity in bulk semiconductors and two-dimensional materials, Reports on Progress in Physics **83**, 036501 (2020).

[34] A. Pilotto, P. Khakbaz, P. Palestri, and D. Esseni, Semiclassical transport in MoS2 and MoS2 transistors by a monte carlo approach, Solid-State Electronics **192**, 108295 (2022).

[35] K. Kaasbjerg, K. S. Thygesen, and K. W. Jacobsen, Phonon-limited mobility in n-type single-layer MoS_2 from first principles, Physical Review B **85**, 10.1103/physrevb.85.115317 (2012).

[36] A. Konar, T. Fang, and D. Jena, Effect of high-κ gate dielectrics on charge transport in graphene-based field

effect transistors, Physical Review B **82**, 10.1103/physrevb.82.115452 (2010).
[37] A. Hauber and S. Fahy, Scattering of carriers by coupled plasmon-phonon modes in bulk polar semiconductors and polar semiconductor heterostructures, Physical Review B **95**, 10.1103/physrevb.95.045210 (2017).
[38] K. Kaasbjerg, K. S. Thygesen, and K. W. Jacobsen, Phonon-limited mobility in n-type single-layer mos 2 from first principles, Physical Review B **85**, 115317 (2012).
[39] M. V. Fischetti and S. E. Laux, Long-range coulomb interactions in small si devices. part i: Performance and reliability, Journal of Applied Physics **89**, 1205 (2001).
[40] B. Radisavljevic and A. Kis, Mobility engineering and a metal–insulator transition in monolayer MoS2, Nature Materials **12**, 815 (2013).
[41] K. K. H. Smithe, C. D. English, S. V. Suryavanshi, and E. Pop, High-field transport and velocity saturation in synthetic monolayer MoS_2, Nano Letters **18**, 4516 (2018).
[42] N. Smith, Classical generalization of the drude formula for the optical conductivity, Physical Review B **64**, 10.1103/physrevb.64.155106 (2001).
[43] T. L. Cocker, D. Baillie, M. Buruma, L. V. Titova, R. D. Sydora, F. Marsiglio, and F. A. Hegmann, Microscopic origin of the drude-smith model, Physical Review B **96**, 10.1103/physrevb.96.205439 (2017).
[44] S. Park, N. Mutz, T. Schultz, S. Blumstengel, A. Han, A. Aljarb, L.-J. Li, E. J. W. List-Kratochvil, P. Amsalem, and N. Koch, Direct determination of monolayer mos_2 exciton binding energies on insulating and metallic substrates, 2D Materials **5**, 025003 (2018).
[45] S. Golovynskyi, O. I. Datsenko, D. Dong, Y. Lin, I. Irfan, B. Li, D. Lin, and J. Qu, Trion binding energy variation on photoluminescence excitation energy and power during direct to indirect bandgap crossover in monolayer and few-layer mos_2, The Journal of Physical Chemistry C **125**, 17806 (2021).

STATEMENTS AND DECLARATIONS

Funding

The authors gratefully acknowledge support by the NSF ECCS award 2212011 (SM; TMD electronic structure and transport) and by the DOE BES award DE-SC0023178 (LA; electrodynamics and multiphysics code development). Preliminary work was supported by the DOE BES award DE-SC0008712 (LA) and by the Splinter Professorship (IK). This work was performed using the compute resources and assistance of the UW-Madison Center for High Throughput Computing (CHTC) in the Department of Computer Sciences.

Competing Interests

The authors have no relevant financial or non-financial interests to disclose.

Author Contributions

SM calculated electronic structure and transport. LA develeoped the electrodynamics solver and some of the multiphysics code. SM and IK conceptualized the paper and wrote the initial draft. All authors contributed to data analysis and writing. All authors read and approved the final manuscript.

Data Availability

Data available upon reasonable request.